Nanoscale

PAPER

View Article Online
View Journal | View Issue

Cite this: *Nanoscale*, 2022, **14**, 6349

Core–shell TiO_{2-x}-Cu_yO microspheres for photogeneration of cyclic carbonates under simulated sunlight†

Jeannie Z. Y. Tan, * Stelios Gavrielides and M. Mercedes Maroto-Valer

Received 6th December 2021,
Accepted 4th April 2022

DOI: 10.1039/d1nr08023g

rsc.li/nanoscale

Propylene carbonates are important organic solvents and feedstocks for different applications, including synthesis of polymers and Li-batteries. The generation of propylene carbonate utilising anthropogenic CO_2 and renewable solar energy offers an alternative sustainable process with a closed loop carbon cycle. The development of microstructured photocatalysts with desired properties, including high degree of product selectivity, wide range of optical properties, and maximised conversion yield, plays an important role for effective production of propylene carbonate from CO_2. A hierachical hollow core with a double shell of TiO_{2-x}-Cu_2O-CuO was fabricated using the versatile solvothermal-microwave synthesis method. The fabricated sample revealed effective cascading of photogenerated electrons and holes that promoted the conversion of propylene carbonate (*i.e.*, 1.6 wt%) under 1 Sun irradiation.

1 Introduction

Continuous development in nanomaterials research has been inspired by the search of new applications, performance development, and combined functionality in a single geometry. The construction of multifunctional nanomaterials in a single geometry has been achieved through surface coating, creating a new class of substances designated as core–shell nanoparticles.[1] The physical and chemical properties of core–shell nanoparticles are mainly associated with the materials and structure of the core and shell, but they are also associated with the interface. A recent finding revealed that the core–shell with raspberry-like structures could maximise the interaction between the core Cr_2O_3 and shell Ti_4O_7 that is beneficial for the separation of photogenerated electron–hole pairs, and thereby, promoting the photoreduction of CO_2 into CH_4.[2]

Titanium dioxide (TiO_2) has been extensively explored as a photocatalyst because of its abundant availability, non-toxicity, and photocorrosion resistance. Unfortunately, the large bandgap of TiO_2 (*i.e.*, 3.2 eV) limits its absorption to the UV region, and therefore, utilising only 4% of the entire solar spectrum.[3] To enhance using a greater portion of the solar spectrum energy while maintaining the commendable properties of TiO_2,[4] various approaches have been proposed, such as introduction of surface heterostructures,[4,5] anion doping,[6,7] loading of metals,[8–10] and coupling of small bandgap semiconductors. Composites of Cu_xO and TiO_{2-x} have been reported and used for different photocatalytic applications, such as hydrogen evolution,[11] CO_2 photoreduction[12,13] and photodegradation of volatile organic compounds.[14]

The use of renewable energy and anthropogenic CO_2 to generate valuable organic chemicals, including carbonates and polycarbonates, has been reported.[15–17] Using solar energy is a sustainable and emerging approach for the generation of value-added polymers because reactions can be performed at low temperature and pressure, and thus, minimizing the environmental impact.[18] To date, the photocatalytic production of cyclic carbonates from CO_2 using rare and costly metals (*i.e.*, Co, Ru) titania-based photocatalysts has been reported in a few studies.[9,19] Although these studies revealed superior selectivity and production yield with respect to the pristine titania and benchmark P25, there is still a need to identify less expensive and more abundant metals as co-catalyst for cyclic carbonate production under mild reaction conditions.

Agglomeration within a photocatalyst has been shown to have a detrimental effect in the photocatalysis reaction due to the formation of recombination centres and reduction of surface area.[20,21] The fabrication of core–shell nanostructures has revealed an enhanced dispersibility and hinders the agglomeration of the photocatalysts and co-catalysts.[22,23] Recently, microwave-assisted synthesis of core–shell materials is gaining attention owing to the rapid and versatility of microwave approach.[24] Using the two-step process of solvothermal followed by microwave treatment, the fabricated core–shell

Research Centre for Carbon Solutions (RCCS), Heriot-Watt University, Edinburgh EH14 4AS, UK. E-mail: j.tan@hw.ac.uk

†Electronic supplementary information (ESI) available: Chronoamperometric analysis and SEM of TiO_{2-x}. See DOI: https://doi.org/10.1039/d1nr08023g

metal oxide microspheres exhibited porous structure attributing to the self-assembled TiO_{2-x} nanoparticles. When the Cu_yO shell layer was incorporated, each TiO_{2-x} nanoparticle was evenly coated, resulting efficient charge transfer for enhanced photogeneration of propylene carbonates even at mild conditions compared to that of industrial.

2 Experimental

2.1 Chemicals

Absolute ethanol (ACS reagent), $K_2C_4TiO_9{\cdot}2H_2O$ (≥98.0%), tetraethyl orthosilicate (TEOS, 98%), diethylene glycol (DEG, ≥99.5%), 2-propanol (anhydrous, 99.5%), copper(II) acetate (99.99%), propylene oxide (PO, 99%), 4-dimethylaminopyridine (DMAP, ≥99%), dichloromethane (CH_2Cl_2 anhydrous, ≥99.8%), Chloroform-D (≥99.8 atom%, anhydrous), NH_3 (28 wt%), NaOH (pellets EMPLURA®) and HCl (37 wt%) were all purchased from Sigma-Aldrich. All the reagents were used as received. Milli-Q water was collected from a Millipore purification system with resistivity 18.2 MΩ cm.

2.2 Method

2.2.1 Synthesis of yellow titania microspheres. Typically, 0.6 g of $K_2C_4TiO_9$ and 300 mL of H_2O were mixed and stirred until a clear solution was obtained. Then, 450 mL of DEG and 2-propanol, respectively, were added and stirred until a homogeneous yellow solution was obtained. The solution was then transferred into the 100 mL Teflon-lined stainless-steel autoclaves and treated at 190 °C for 12 h. After the hydrothermal treatment, a yellowish orange powder was obtained that was then washed three times with ethanol and water (alternating sequence), respectively. After drying the powder obtained in an oven at 75 °C, the product (denoted as TiO_{2-x}, 0.06 g) was calcined at 500 °C with ramping 1 °C min^{-1} and maintained at 500 °C for 4 h.

2.2.2 Synthesis of TiO_{2-x}/SiO_2 microspheres. The synthesis of TiO_{2-x}/SiO_2 microspheres was prepared according to a previous study.[22] Briefly, an ethanol dispersion of TiO_{2-x} microspheres (1.2 mL, 0.05 g mL^{-1}) was added into a round bottom flask containing ethanol (112 mL), Milli-Q water (28 mL) and NH_3 (2.0 mL, 28 wt%) under ultrasound for 30 min (solution A). After that, 1.6 mL of TEOS was added into the solution A with a flow rate 0.4 mL min^{-1}. Then, the solution was kept under continuous mechanical stirring for 12 h at room temperature. The resultant TiO_{2-x}/SiO_2 microspheres were separated using a centrifuge (ThermoFisher Sorvall Biofuge Primo Benchtop Centrifuge, 11 000 rpm for 15 min), followed by washing three times with of Milli-Q water and absolute ethanol (alternating sequence), respectively.

2.2.3 Synthesis of $TiO_{2-x}/SiO_2/Cu_xO$ microspheres. The product of TiO_{2-x}/SiO_2 microspheres obtained was re-dispersed into ethanol (76 mL) and mixed with concentrated NH_3 (0.35 mL, 28 wt%) under ultrasound for 30 min (solution B). 12.2 mL of Cu-precursor with different concentration (*i.e.*, 12.5, 25, 50 mM, denoted as TC-*x*, in which *x* is the concentration in mM), which was prepared using copper(II) acetate and ethanol (solution C), was added into solution B with a flow rate of 0.4 mL min^{-1}, producing solution D. After stirring for 30 min, 3.0 mL of NaOH (0.1 M) was added into solution D and left stirring for 1 h. Then, the solution was transferred into a sealed vessel for microwave treatment (150 °C for 45 s using Discover 2.0 by CEM Corporate) to synthesize the Cu_xO layer onto TiO_{2-x}/SiO_2. The resulted $TiO_{2-x}/SiO_2/Cu_xO$ microspheres were separated using centrifuge (11 000 rpm for 15 min), followed by washing with three times of Milli-Q water and absolute ethanol (alternating sequence), respectively.

2.2.4 Removal of SiO_2 barrier. The TiO_{2-x}/Cu_xO microspheres were synthesized using an alkaline hydrothermal etching assisted crystallisation method. The $TiO_{2-x}/SiO_2/Cu_xO$ product obtained in the previous step was mixed with an aqueous NaOH solution (20 mL, 1.0 M), then the solution was transferred to a 100 mL Teflon-lined stainless-steel autoclave. The autoclave was heated at 150 °C for 24 h, and then allowed to cool down to room temperature. Then, the product obtained was immersed in aqueous HCl (100 mL, 0.1 M) for 20 min, and subsequently washed with Milli-Q water until pH value was close to 7 to avoid any residue Cl^- or salt formation in the sample. Last, the sample was dried at 75 °C overnight.

2.2.3 Synthesis of TiO_{2-x}/Cu_xO (without core–shell microstructure). TiO_{2-x} microspheres (1.2 mL, 0.05 g mL^{-1}) was added into a round bottom flask containing ethanol (112 mL), Milli-Q water (28 mL) and NH_3 (2.0 mL, 28 wt%) under ultrasound for 30 min (solution A). After that, 12.2 mL of Cu-precursor (*i.e.*, 25 mM) was added into solution A with a flow rate of 0.4 mL min^{-1}. Then, the solution was transferred into a sealed vessel for microwave treatment (150 °C for 45 s using Discover 2.0 by CEM Corporate) to synthesize sample $TC\text{-}25^{direct}$, which was separated from the precursor solution using centrifuge (11 000 rpm for 15 min), followed by washing with three times of Milli-Q water and absolute ethanol (alternating sequence), respectively.

2.3 Characterisation

The morphology of the synthesized products was examined by a field emission scanning electron microscopy (FE-SEM, Quanta 200 F FEI), a high-resolution transmission electron microscope (HRTEM, FEI Titan Themis 200) equipped with an energy-dispersive X-ray spectroscopy (EDX) detector operated at 200 kV. To investigate the interior structures of the nanospheres, samples were embedded in TAAB 812 resin and sliced into ~90 nm thick sections. The sliced sections were mounted on the TEM Ni grid. Surface area analysis was performed on Micromeritics ASAP 2420 Surface Area and Pore Analyser. The measurement was recorded using N_2 (99.999%) at 77 K. Crystallinity and phase identification of the synthesized products were conducted using powder X-ray diffraction XRD (Bruker D8 Advanced Diffractormeter) equipped with Cu Kα radiation (λ = 1.5418 Å) and compared with the ICDD–JCPDS powder diffraction file database. Diffuse reflectance spectra were collected using a UV-vis spectrometer (Perkin-Elmer Lambda 900) equipped with an integrating sphere (150 mm). X-ray photoelectron spectrum (XPS) analysis was performed using a Thermo Fisher Scientific NEXSA spectrometer. The samples were analysed

using a micro-focused monochromatic Al X-ray source (19.2 W) over an area of approximately 100 microns. Data were recorded at pass energies of 200 eV for survey scans and 50 eV for high resolution scan with 1 eV and 0.1 eV step sizes, respectively. Charge neutralisation of the sample was achieved using a combination of both low energy electrons and argon ions. C 1s electron at 284.8 eV was used as standard reference to calibrate the photoelectron energy shift. All the data analysis was performed on the CasaXPS software (version: 2.3.20rev1.0). The chronoamperometric measurement was carried out on the Autolab PGSTAT 302N electrochemical workstation with a standard three–electrode system. A solar simulator (HAL-320 by Asahi Spectra USA; AM 1.5G; 100 mW cm^{-2}) was used as the light source (100 mW cm^{-1}, 350–1100 nm). To fabricate the working electrode, 1 mg of powder sample was dispersed in 0.5 mL of ethanol followed by sonication for 15 min. The solution obtained was drop-casted onto a piece of fluorine doped tin oxide (FTO) glass to coat an area with dimension 1 cm × 1 cm. Then, the prepared film was air dried and annealed at 200 °C for 1 h. Pt wire and Ag/AgCl (KCl 1 M) were used as the counter and reference electrodes, respectively. The electrolyte used was 0.2 M of Na_2HCO_3 aqueous solution. Surface area analysis was performed on a Micromeritics ASAP 2420 Surface Area and Pore Analyser using Brunnaeur, Emmett and Teller (BET) analysis to work out surface area from the shape of the pressure *vs.* Nitrogen adorption plot.

2.4 Photocatalytic testing

Photogeneration of propylene carbonate (PC) from PO was conducted in a customised stainless steel photoreactor with a quartz window as shown in our recent publication.[9] 0.01 g of sample was distributed as powder into the reacting solution, which contained 200 mL of PO, 25 mL of dichloromethane and 0.23 of DMAP. The reacting solution was left stirring overnight before light irradiation. The reaction was performed under the optimised conditions (CO_2 at 200 kPa and 55 ± 2 °C) within a closed reactor filled, controlled by a hot plate placed and monitored using a digital thermometer (RS-41) connected with the reactor throughout the experiment for 5 h. A solar simulator (HAL-320 by Asahi Spectra USA; AM 1.5G; 100 mW cm^{-2}) was used as the light source (100 mW cm^{-1}, 350–1100 nm). After the reaction, the solution was filtered using a filter funnel to remove the powdered sample. Then, the product was purified using a rotary evaporator (Sturt RE300, 60 °C, 50 rpm). The purified solution was added with 1.0 mL of Chloroform-D and then analysed using 1H-Nuclear magnetic resonance (NMR) spectroscopy (Bruker AV400). The optimised sample (*i.e.*, TC-25) was also tested under the same experimenting conditions in the absence of light (denoted as TC-25^{dark}). Catalyst cycling test was performed using the recovered catalyst in a fresh reacting solution under the same experimenting conditions. This step was repeated 3 times. The conversion yield of the fabricated samples was calculated using the equation below:

$$\text{Conversion-yield} = \frac{\text{products obtained after purification (g)}}{\text{weight of PO solution (g)}} \times 100\%$$

3 Results and discussion

The core–shell TiO_{2-x}-Cu_yO samples, which were fabricated using the solvothermal-microwave approaches, revealed high crystallinity and dispersive nanoparticles, as shown in Fig. 1A and B, respectively. The pristine TiO_{2-x} exhibited only anatase phase (JCPDS Card No.: 21-1272). When Cu_yO was loaded as the shell layer, the XRD signal of anatase phase was gradually reduced with the increase of Cu-precursor concentration from 12.5–50 mM (Fig. 1A). This was probably due to the increase of the Cu_yO shell layer. In addition, weak signals of Cu_2O (JCPDS Card No.: 65-3288) and/or CuO (JCPDS Card No.: 44-0706) were detected, indicating a small amount of Cu_2O and/or CuO present in the samples. Specifically, the sample treated with low concentration of Cu-precursor (*i.e.*, 12.5 and 25 mM) showed a weak signal of Cu_2O (Fig. 1A-b and c). When the concentration of Cu-precursor increased to 50 mM, the signal of CuO emerged (Fig. 1A-d).

The optical properties of the fabricated samples were analysed using the Kubelka–Munk function (Fig. 1B) derived from diffused reflectance (Fig. S1†). The fabricated TiO_{2-x} and the samples with Cu_2O (*i.e.*, TC-12.5 and TC-25) exhibited approximately 3.2 eV of band gap. The band gap energy of TC-12.5 and TC-25 was not significantly reduced after the loading of Cu_2O, which has a band gap of ~2.4 eV, probably due to the small amount of Cu_2O.[25] When the Cu-precursor concentration was increased to 50 mM, the band gap was reduced to 2.7 eV. This was due to the presence of CuO, which has a smaller band gap (~2.2 eV) than Cu_2O.[25] The estimated band gap energy was not dominated by Cu_yO, suggesting highly dispersed Cu_yO coating around the TiO_{2-x} nanoparticles. This observation is further discussed later using the results from the SEM and HRTEM studies.

The fabricated samples were tested for PC production under solar simulator (Table 1). Sample TiO_{2-x} converted 0.1 wt% of PO into PC. When Cu_yO was incorporated as the shell layer, the conversion yield increased significantly. Sample TC-25 achieved the highest conversion yield of 1.6 wt%. P25 as the benchmark photocatalyst, samples TC-25^{dark} and TC-25^{direct} converted only trace amount of product. The product selectivity of the fabricated samples achieved 100% as shown in the NMR (Fig. S2†). The performance of the fabricated samples was further analysed and discussed using various characterisation techniques, including photocurrent measurements, HRTEM, and XPS analysis.

The electronic properties of the fabricated samples were investigated by performing chronoamperometric analysis (Fig. S4†). P25 exhibited the lowest photocurrent among the samples (Fig. S4a†), whereas the fabricated TiO_{2-x} exhibited almost 10 times higher in the photocurrent measurement (S4b†). When Cu_yO was loaded as the shell layer, sample TC-12.5 revealed a significant increase in the photocurrent upon the irradiation of solar simulator (Fig. S4c†). Raising further the concentration of Cu-precursor to 25 mM, the photocurrent was increased ~50% (Fig. S4d†). When the concentration was increased to 50 mM, a detrimental effect was

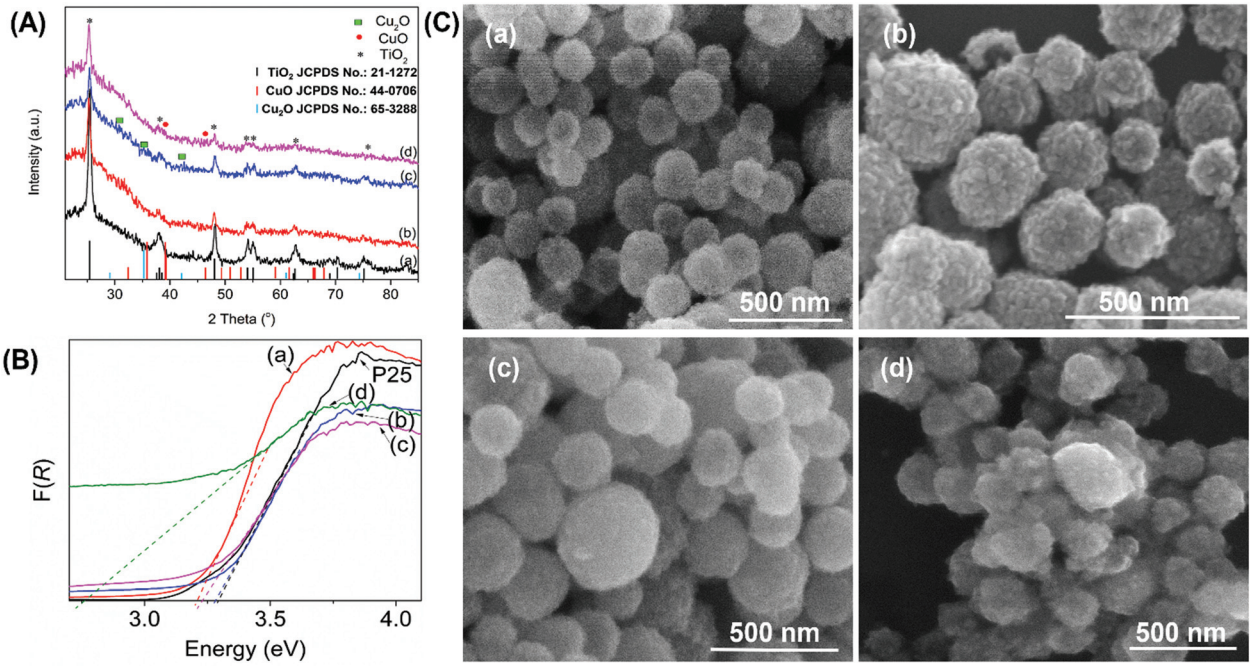

Fig. 1 XRD (A), Kulbelka–Munk plot (B) and SEM (C) of TiO_{2-x} (a), TC-12.5 (b), TC-25 (c), TC-50 (d). The Kubelka–Munk of P25 is included in (B) as labelled.

Table 1 Yield obtained from the conversion of PO into PC utilising the fabricated samples

Sample name	Composition (Cu : Ti) XPS	HRTEM	Conversion yield (wt%)
TiO_{2-x}	—	—	0.1
TC-12.5	0.003	0.089	1.0
TC-25[a]	0.011	0.171	1.6
TC-50	1.734	0.402	0.8
P25	—	—	Trace
$TC\text{-}25^{dark}$	0.011	0.171	Trace
$TC\text{-}25^{direct}$	0.015	0.289	Trace

[a] Cycling tests were conducted. Further discussion and evidence can be found in ESI (Fig. S3†).

observed (Fig. S4e†). Hence, the trend observed in the chronoamperometric analysis explained the performance of the photocatalysts in PC generation.

To obtain an insight of the physical and electronic properties of the fabricated samples, SEM and TEM analysis were performed. The morphology of the pristine TiO_{2-x} nanoparticles, which was fabricated using the solvothermal method, featured a rough surface and possessed a diameter of ~200 nm (Fig. 1C-a). The microtomed TiO_{2-x} sample exhibited an interesting microstructure under TEM, in which each particle was made up from many small nanoparticles (Fig. S5†), that showed a bimodal pore size distribution in the mesoporous range (*i.e.*, ~15 and ~30 nm) with a surface area of 76 $m^2\ g^{-1}$ (Fig. S6†). This self-assembled microstructure was proposed to minimize the bulk recombination of photogenerated electron–hole pairs, resulting in enhanced electronic properties, as shown in Fig. S3.† When 12.5 mM of Cu-precursor was employed to synthesize the shell layer, the rough surface feature was still observable in TC-12.5 sample (Fig. 1B-b). When the concentration of Cu-precursor increased to 25 mM, the surface of the nanoparticles became smoother than for sample TC-12.5 (Fig. 1C-c), indicating that the increase of Cu-precursor concentration led to a thicker Cu_yO layer as well as optimising the coating on each of the TiO_{2-x} nanoparticles within the microsphere (Further discussed with HRTEM). Further increasing the concentration of Cu-precursor to 50 mM resulted severe agglomeration (*i.e.*, TC-50 sample, Fig. 1C-d).

The microstructure of the fabricated samples TC-12.5 and TC-25 was further investigated using HRTEM. The element distribution and the formed core–shell structured nanoparticles were analysed after microtoming. The microtomed samples revealed a porous structure (Fig. 2). Sample TC-12.5 (Fig. 2a) exhibited a thin and homogeneous layer of Cu (Fig. 2b), and the O (Fig. 2c) and Ti (Fig. 2d) appeared as a 'donut-shape', having a void in the middle of the nanoparticle. The bimodal distribution of the pore size of this sample was shifted from ~15 and ~30 nm (*i.e.*, sample TiO_{2-x}) to ~8 and ~40 nm with an slight surface area reduction (*i.e.*, 73 $m^2\ g^{-1}$, Fig. S4†) compared to pristine TiO_{2-x}. The reduction of pore size was attributed to the loading of Cu_yO; whereas the increase was associated with void formation. When the Cu-precursor concentration increased, the amount of Cu increased significantly (Fig. 2h). The elemental mapping of Cu exhibited a high dis-

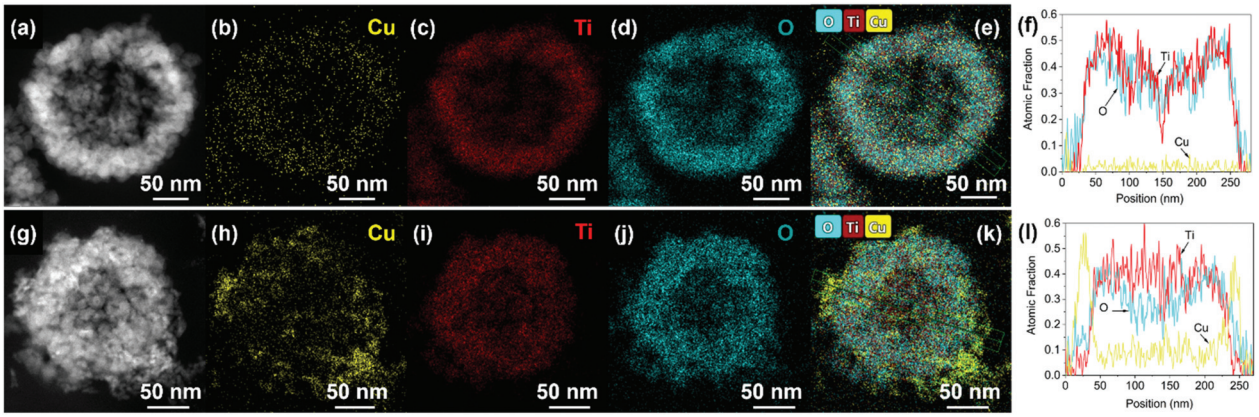

Fig. 2 HRTEM images (a and g) and Cu (b and h), O (c and i), Ti (d and j), combined mapping (e and k) and line scan (f and l) of TC-12.5 and TC-25, respectively.

persion of Cu within the microsphere. This observation revealed a novel core–shell structure, in which the shell Cu_yO layer coated on each TiO_{2-x} nanoparticles within the microspheres. In additional, the void appeared on TC-25 tended to be smaller than TC-12.5 sample as shown in the line scan analysis (Fig. 2f and l). As a result, a unimodal pore size distribution (*i.e.*, ~21 nm) was observed in this sample (Fig. S4†). The homogeneity of pore size distribution also led to enhanced surface area (*i.e.*, 88 $m^2\ g^{-1}$) when compared to samples TiO_{2-x} and TC-12.5, resulting the highest conversion among the fabricated samples. Further increasing the concentration of Cu-precursor to 50 mM, the surface area reduced significantly to 34 $m^2\ g^{-1}$ because of severe agglomeration as observed under SEM (Fig. 1C-d).

Based on the observations above, a synthesis mechanism was proposed in which the formation of void within the TC nanoparticles was due to the influx of highly concentrated NaOH aqueous solution into the nanoparticles during the hydrothermal treatment to remove the SiO_2 barrier layer (refer to Experimental section 2.2.4). The highly concentrated NaOH broke some of the Ti–O bonds under the autogeneous pressure within the autoclave, leading to the dissolution of TiO_{2-x}.[26] Due to the small size of TiO_{2-x}, the dissolution could be achieved easily. However, the outflow of dissolved titania was unfortunately restricted by the Cu_yO shell layer, causing imbalanced mass transport, which is known as the Kirkendall effect.[27] As a result, re-crystallisation of TiO_{2-x} occurred within the nanoparticles, forming a double shell with a hollow core. When the thickness of Cu_yO increased, the outflow of dissolved titania was restricted, and re-crystallisation of TiO_{2-x} occurred immediately, resulting in less and smaller voids than those observed in the sample with thinner Cu_yO layer (*i.e.*, TC-12.5 sample).

The chemical composition of Cu and Ti was analysed using XPS and EDX-HRTEM. The values obtained using these two techniques were significantly different due to different depth of analysis. Specifically, the quantitative EDX-HRTEM measurement represented the bulk sampling focusing on only one microsphere (Fig. 2a and e), whereas XPS analysis revealed only the surface chemical composition because the sampling depth was ~5 nm. As a result, the XPS measured Cu : Ti ratio of TC-50, which had thick and excessive Cu_yO, was >1, which is incorrect.

XPS analysis was also performed to acquire information regarding the surface state of the fabricated sample (Fig. 3). TiO_{2-x} exhibited a typical titania pattern, in which the difference of Ti $2p_{3/2}$ (458.4 eV) and $2p_{1/2}$ (464.1 eV) peaks was approximately 5.7 eV (Fig. 3A-a). The separation of peaks remained the same in the fabricated TC samples. However, the peaks in all fabricated TC samples moved to a higher binding energy (*i.e.*, Ti $2p_{3/2}$ and $2p_{1/2}$ centred at 458.9 and 464.6 eV, respectively) compared to pristine TiO_{2-x}. The shift in the position of these peaks indicated the Cu addition affected the electronic state of Ti element; probably some of the Ti ions were substituted with Cu ions in the lattices after the dissolution recrystallisation reaction, forming the Ti–O–Cu structure. In addition, the intensity of Ti 2p peaks decreased with the increase of Cu-precursor concentration. This was because the average depth of analysis for an XPS measurement is approximately 5 nm,[28] the thicker Cu_yO layer revealed a weaker Ti 2p peak intensity.

The O 1s binding energy of the fabricated samples shifted to higher binding energy with the increase of Cu-precursor concentration (Fig. 3B). Sample TiO_{2-x} exhibited 2 deconvoluted areas, including the dominant peak centred at 531.1 eV and a shoulder peak at higher binding energy (532.7 eV), indicating the presence of oxygen vacancy within the sample (Fig. 3B-a).[29] When the Cu-layer was incorporated into the sample, the area of the shoulder peak (532.7 eV) increased with the concentration of Cu-precursor from 12.5 to 25 mM (Fig. 3B-b and c, respectively). When the highest concentration of Cu-precursor (50 mM) was employed, only a peak emerged at 532.7 eV (Fig. 3B-d). This was because the thickness of Cu_yO had exceeded the analysis depth of XPS (~5 nm), and thus, the data acquired was only from the shell layer of Cu_yO, as shown in Table 1.

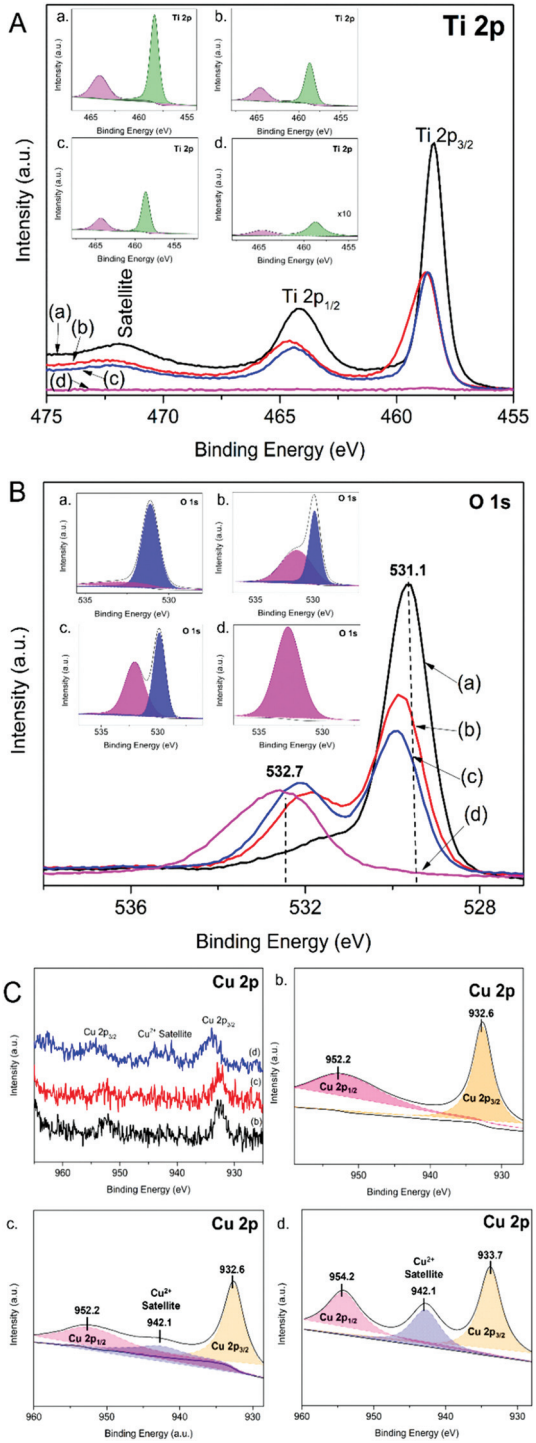

Fig. 3 High resolution XPS spectra of Ti 2p (A), O 1s (B) and Cu 2p (C)* for the samples of TiO_{2-x} (a), TC-12.5 (b), TC-25 (c), TC-50 (d). *TiO_{2-x} (a) does not possess Cu element.

High resolution Cu 2p spectra evidenced the presence of Cu_yO in the fabricated TC samples (Fig. 3C). Sample TC-12.5 exhibited the characteristic pattern of Cu_2O, in which the Cu $2p_{3/2}$ and $2p_{1/2}$ positioned at 932.6 and 952.2 eV, respectively (Fig. 3C-b).[30] When the Cu-precursor concentration increased

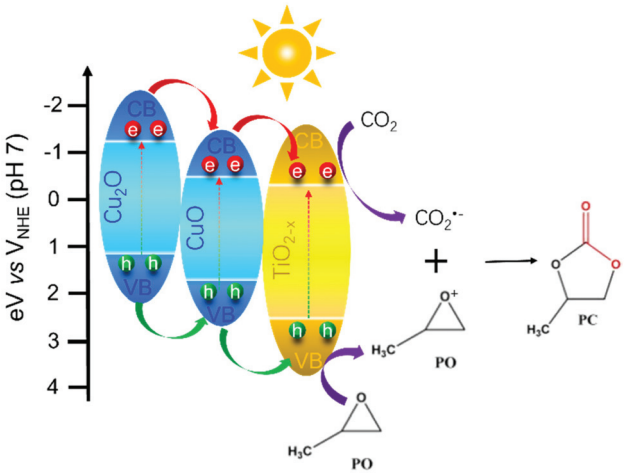

Scheme 1 Illustrative diagram of the proposed working mechanism for the photocatalytic generation of PC from PO.

to 25 mM, the position of Cu $2p_{3/2}$ and $2p_{1/2}$ remained. In addition, a very weak satellite peak (~942.1 eV) was observed, evidencing the presence of Cu^{2+}.[31] Hence, Cu_2O and CuO co-existed in the sample TC-25. Further increasing the concentration to 50 mM, the Cu $2p_{3/2}$ and $2p_{1/2}$ shifted to higher binding energy (*i.e.*, 933.7 and 954.2 eV, respectively), proving the formation of CuO.[32] Meanwhile, the peak area of Cu^{2+} increased significantly. These observations confirmed that only CuO was present in sample TC-50.[32]

Based on the information obtained from various characterisation analysis, a working mechanism of the photocatalytic reaction was proposed (Scheme 1). The results obtained revealed that the co-existence of Cu_2O and CuO in sample TC-25 was an important characteristic to achieve the highest conversion yield into PC. During the photocatalytic reaction, electron–hole pairs were separated into conduction and valence bands, respectively, in the semiconductors. The electrons in Cu_2O, which positioned at the highest V_{NHE}, moved to the conduction band of CuO that positioned at slightly lower V_{NHE}. The electrons accumulated in the conduction band of CuO again moved to the conduction band of TiO_{2-x}. The holes remaining in the valence band of the semiconductors proceeded in the same direction to the photogenerated electrons. The accumulated holes in the valence band of titania then oxidised the PO to PO^+. The unique microstructure of TC-25 provides an effective cascading of the electrons and holes, thus, promoting the activation of CO_2 and PO molecules, and the subsequent addition reaction to produce PC.

4 Conclusions

The versatile 2-step synthesis process of solvothermal and microwave approaches had successfully fabricated porous double shell of TiO_{2-x} and Cu_yO nanoparticles with hollow core as a result of the Kirkendall effect. The bulk and surface

analysis revealed that Cu_yO was successively coated onto each titania nanoparticle within the microspheres. Various concentration of Cu-precursor (12.5–50 mM), which was employed to control the thickness of the shell Cu_yO layer, had also caused the change of Cu^+ to Cu^{2+}. The optimised sample, which was fabricated using 25 mM of Cu-precursor that resulted the bulk Cu : Ti ratio of 0.171, exhibited the conversion yield of 1.6 wt% for 4 h under 1 sun irradiation. The porous structure and the synergistic effect of Cu_2O and CuO as the outer shells of the nanoparticles exhibited an effective transportation of the photogenerated electro-hole pairs, allowing the conversion of PO into PC.

Author contributions

Jeannie Z. Y. Tan – Data collection, first draft writer, editing and submission. Stelios Gavrielides – NMR analysis and editing. M. Mercedes Maroto-Valer – Supervision and draft reviewing.

Conflicts of interest

There are no conflicts to declare.

Acknowledgements

The authors thank the financial support provided by the Engineering and Physical Sciences Research Council (EP/K021796/1) and the Research Centre for Carbon Solutions (RCCS) at Heriot-Watt University. The electron microscopy facility in the School of Chemistry, University of St Andrews, which is supported by the EPSRC Capital for Great Technologies Grant EP/L017008/1, is acknowledged. XPS data collection was performed at the EPSRC National Facility for XPS ('HarwellXPS'), operated by Cardiff University and UCL, under contract no. PR16195.

Notes and references

1 Y. Hou, X. Wang, Y. Guo and X. Zhang, *Nanoscale*, 2021, **13**, 18695–18701.
2 J. Z. Y. Tan, F. Xia and M. M. Maroto-Valer, *ChemSusChem*, 2019, **12**, 5246–5252.
3 N. Shehzad, M. Tahir, K. Johari, T. Murugesan and M. Hussain, *J. CO_2 Util.*, 2018, **26**, 98–122.
4 M. Wang, J. Ioccozia, L. Sun, C. Lin and Z. Lin, *Energy Environ. Sci.*, 2014, **7**, 2182–2202.
5 M. Ge, C. Cao, J. Huang, S. Li, Z. Chen, K.-Q. Zhang, S. S. Al-Deyab and Y. Lai, *J. Mater. Chem. A*, 2016, **4**, 6772–6801.
6 R. Asahi, T. Morikawa, T. Ohwaki, K. Aoki and Y. Taga, *Science*, 2001, **293**, 269–271.
7 X. Wang, M. Blackford, K. Prince and R. A. Caruso, *ACS Appl. Mater. Interfaces*, 2012, **4**, 476–482.
8 D. Kong, J. Z. Y. Tan, F. Yang, J. Zeng and X. Zhang, *Appl. Surf. Sci.*, 2013, **277**, 105–110.
9 S. Gavrielides, J. Z. Y. Tan, E. S. Fernandez and M. M. Maroto-Valer, *Faraday Discuss.*, 2019, **215**, 407–421.
10 S. He, J. Huang, J. L. Goodsell, A. Angerhofer and W. D. Wei, *Angew. Chem., Int. Ed.*, 2019, **58**, 6038–6041.
11 K. Lalitha, G. Sadanandam, V. D. Kumari, M. Subrahmanyam, B. Sreedhar and N. Y. Hebalkar, *J. Phys. Chem. C*, 2010, **114**, 22181–22189.
12 S.-I. In, D. D. Vaughn II and R. E. Schaak, *Angew. Chem., Int. Ed.*, 2012, **51**, 3915–3918.
13 M. A. Ávila-López, S. Gavrielides, X. Luo, A. E. Ojoajogwu, J. Z. Y. Tan, E. Luévano-Hipólito, L. M. Torres-Martínez and M. M. Maroto-Valer, *J. CO2 Util.*, 2021, **50**, 101588.
14 X. Qiu, M. Miyauchi, K. Sunada, M. Minoshima, M. Liu, Y. Lu, D. Li, Y. Shimodaira, Y. Hosogi, Y. Kuroda and K. Hashimoto, *ACS Nano*, 2012, **6**, 1609–1618.
15 Q. Zhu, *Clean Energy*, 2019, **3**, 85–100.
16 A. Mustafa, B. G. Lougou, Y. Shuai, Z. Wang and H. Tan, *J. Energy Chem.*, 2020, **49**, 96–123.
17 X. Yang, C. Ren, X. Liu, P. Sun, X. Xu, H. Liu, M. Shen, S. Shang and Z. Song, *Mater. Chem. Front.*, 2021, **5**, 6160–6170.
18 S. Das and W. M. A. Wan Daud, *RSC Adv.*, 2014, **4**, 20856–20893.
19 P. K. Prajapati, A. Kumar and S. L. Jain, *ACS Sustainable Chem. Eng.*, 2018, **6**, 7799–7809.
20 S.-M. Park, A. Razzaq, Y. H. Park, S. Sorcar, Y. Park, C. A. Grimes and S.-I. In, *ACS Omega*, 2016, **1**, 868–875.
21 J. Wang, J. Wan, N. Yang, Q. Li and D. Wang, *Nat. Rev. Chem.*, 2020, **4**, 159–168.
22 W. Li, Y. Deng, Z. Wu, X. Qian, J. Yang, Y. Wang, D. Gu, F. Zhang, B. Tu and D. Zhao, *J. Am. Chem. Soc.*, 2011, **133**, 15830–15833.
23 H. Zhou, S. Xu, D. Zhang, S. Chen and J. Deng, *Nanoscale*, 2017, **9**, 3196–3205.
24 A. A. Womiloju, C. Höppener, U. S. Schubert and S. Hoeppener, *Part. Part. Syst. Charact.*, 2020, **37**, 2000019.
25 D. S. Murali, S. Kumar, R. J. Choudhary, A. D. Wadikar, M. K. Jain and A. Subrahmanyam, *AIP Adv.*, 2015, **5**, 047143.
26 Y. Yang, S. Liao, W. Shi, Y. Wu, R. Zhang and S. Leng, *RSC Adv.*, 2017, **7**, 10885–10890.
27 J. Z. Y. Tan, S. Gavrielides, M. Belekoukia, W. A. Thompson, L. Negahdar, F. Xia, M. Maroto-Valer and A. M. Beale, *Chem. Commun.*, 2020, **56**, 12150–12153.
28 H. Bluhm, in *In Situ Characterization of Thin Film Growth*, ed. G. Koster and G. Rijnders, Woodhead Publishing, 2011, pp. 75–98, DOI: **10.1533/9780857094957.2.75**.
29 B. Bharti, S. Kumar, H.-N. Lee and R. Kumar, *Sci. Rep.*, 2016, **6**, 32355.
30 H. Azimi, S. Kuhri, A. Osvet, G. Matt, L. S. Khanzada, M. Lemmer, N. A. Luechinger, M. I. Larsson, E. Zeira,

D. M. Guldi and C. J. Brabec, *J. Am. Chem. Soc.*, 2014, **136**, 7233–7236.
31 P. Jiang, D. Prendergast, F. Borondics, S. Porsgaard, L. Giovanetti, E. Pach, J. Newberg, H. Bluhm, F. Besenbacher and M. Salmeron, *J. Chem. Phys.*, 2013, **138**, 024704.
32 Y. Wang, Y. Lü, W. Zhan, Z. Xie, Q. Kuang and L. Zheng, *J. Mater. Chem. A*, 2015, **3**, 12796–12803.